A van der Waals heterostructure of $MoS_2/MoSi_2N_4$: a first-principles study

Journal Name

ARTICLE TYPE

Cite this: DOI: 10.1039/xxxxxxxxxx

Van der Waals heterostructure of $MoS_2/MoSi_2N_4$: A First-principle study

A. Bafekry[1,2†], M. Faraji[3], A. Abdollahzadeh[4], M. M. Fadlallah[5], Chuong V. Nguyen[6], M. Ghergherehchi[7], S.A.H. Feghhi[1]

Received Date
Accepted Date

DOI: 10.1039/xxxxxxxxxx

www.rsc.org/journalname

Motivated by the successful preparation of $MoSi_2N_4$ monolayer in the last year [Hong et al., Sci. 369, 670 (2020)], we investigate the structural, electronic and optical properties of $MoS_2/MoSi_2N_4$ heterostructure (HTS). The phonon dispersion and the binding energy calculations refer to the stability of the HTS. The heterostructure has an indirect bandgap 1.26 (1.84) eV using PBE (HSE06) which is smaller than the corresponding value of $MoSi_2N_4$ and MoS_2 monolayers. We find the work function of $MoS_2/MoSi_2N_4$ HTS is smaller than the corresponding value of its individual monolayers. The heterostructure structure can enhance the absorption of light spectra not only in the ultraviolet region but also in the visible region as compared to $MoSi_2N_4$ and MoS_2 monolayers. The refractive index behaviour of the HTS can be described as the cumulative effect which is well described in terms of a combination of the individual effects (the refractive index of $MoSi_2N_4$ and MoS_2 monolayers).

1 Introduction

The capability of 2D novel materials in industrial-grade 2D nanodevices can be remarkably elevated by the tremendous design possibility provided by van der Waals heterostructures (vdWHTSs) in which the physical features can be tuned desirably via vertically stacking various 2D atomic monolayers (MLs) [1–7]. Using vdWHTSs, constructed with stacking two or more 2D atomic thick materials, is considered as one of the best remedies to break the limitations of single-layer materials, where the newly designed vdWHTs put forth a slow electron-hole recombination rate [8–15]. This subject is a matter of interest for nanoelectronic devices owing to lacking dangling bonds, atomically sharp interface and extremely low trap states [16,17]. Vertically designed 2D semiconducting HTS devices have manifested higher operation power and higher processing speed than conventional bulk junctions.

A recent study on the vertically designed HTS of graphene/Ga_2SSe showed that the engineering of interlayer spacing can work efficiently both on controlling the interface contact type and the Schottky-barrier-height of the HTS, which is crucial for performance improvement of the controllable nanoelectronic and optoelectronic devices [18]. Finding graphene ML [19] has triggered enormous efforts to explore novel 2D materials with peculiar physical traits and new performances. For instance, a group of 2D transition metal dichalcogenides (TMDCs), including MoS_2 and WS_2, has drastically changed the world of optoelectronic, photonic and energy devices during the few recent years [20–24].

A novel investigation on the MoS_2/C_3N HTS revealed that the full hydrogenation of the HTS resulted in the tuning of the electronic structure that is very vital for applications in emerging technological devices with precisely controlled properties [25]. In addition to 2D TMDCs, nano dimensional transition metal nitride (TMN) semiconductors have been tremendously studied recently [26–30]. Meanwhile, as an interesting study that has covered both TMDCs and carbon based nitride, the vdWHTs of Janus TMDCs on graphite boron-carbon-nitride nanosheets were studied fundamentally [31]. Their results showed that holly structures of BCN crystals are suitable for HTS formation even over a vdW-type interaction, which significantly changes the electronic nature of the constituent layers. Furthermore, some of the different 2D HTS are reported in previous works [32,32,34–38].

As a new class of air-stable 2D TMN semiconductors, $MoSi_2N_4$

[1]*Department of Radiation Application, Shahid Beheshti University, Tehran, Iran. E-mail: bafekry.asad@gmail.com*
[2]*Department of Physics, University of Antwerp, Groenenborgerlaan 171, B-2020 Antwerp, Belgium.*
[3]*Micro and Nanotechnology Graduate Program, TOBB University of Economics and Technology, Sogutozu Caddesi No 43 Sogutozu, 06560, Ankara, Turkey*
[4]*Nano Research Lab, Lahijan Branch, Islamic Azad University, Lahijan, Iran*
[5]*Department of Physics, Faculty of Science, Benha University, 13518 Benha, Egypt*
[6]*Department of Materials Science and Engineering, Le Quy Don Technical University, Hanoi 100000, Vietnam*
[7]*College of Electronic and Electrical Engineering, Sungkyunkwan University, Suwon, Korea. Email: mitragh@skku.edu*
† *To whom correspondence should be addressed.*

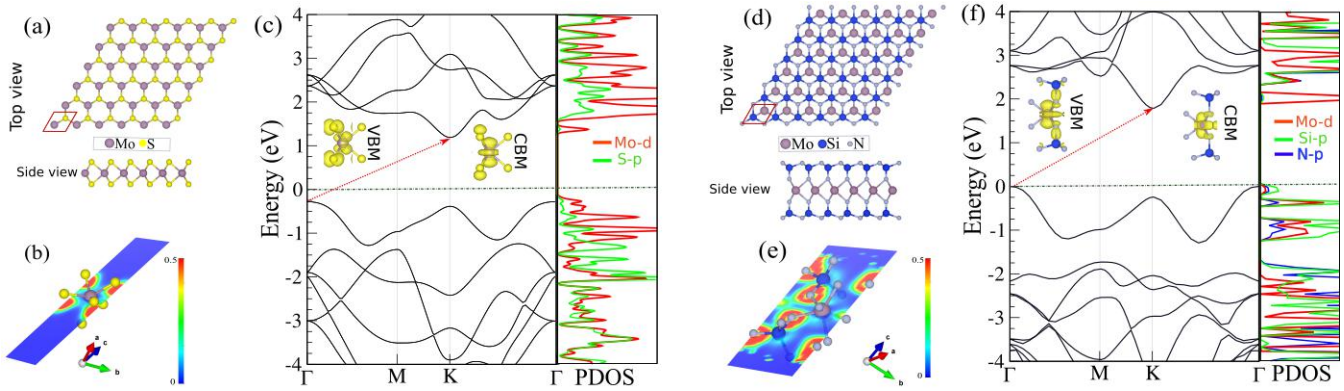

Fig. 1 (a,d) Atomic structures, (b,e) contour plot of the electron localization function (ELF) and (d,f) electronic band and PDOS of MoS_2 (left) and $MoSi_2N_4$ (right) monolayers. The primitive unit cell is indicated by a red hexagonal. Charge density of the valance band maximum (VBM) and conduction band minimum (CBM) orbitals are shown in the inset in electronic structure. The zero of energy is set to Fermi-level.

monolayer shows unique electrical and mechanical properties. However, the air stability of the experimental synthesized 2D TMNs is a big challenge. Recently, W. Ren et al. have managed to synthesis an air-stable 2D $MoSi_2N_4$ monolayer using the chemical vapor deposition (CVD) route[39]. This was achieved by sandwiching an MoN_2 layer between two Si-N bilayers. As a result, an indirect bandgap semiconductor was attained. Bafekry et al.[40] have theoretically studied the structural, mechanical, thermal, electronic and optical properties of the $MoSi_2N_4$ monolayer employing DFT calculations. The physics behind the electrically contacting $MoSi_2N_4$ with metals is still under consideration. Particularly, compared to the 2D transition metal dichalcogenides (TMDCs)/2D-metal contacts that show quite exotic but interesting physical phenomena, the idea of integration of $MoSi_2N_4$ with 2D metals comes to mind. Ang et al.[44] have recently studied the vdWHTs composed of $MoSi_2N_4$ vertically contacted by graphene and NbS_2 MLs using first principles calculation.

In the present study, we introduce a novel VdWHTS of $MoS_2/MoSi_2N_4$. We investigate the related structural, electronic, and optical properties using first principle calculations. The results showed that the HTS has a work function and energy bandgap smaller than its individual monolayers. The optical results show that the HTS can improve the absorption of light in the whole range of light as compared to its individual monolayers.

2 Computational Methods

The plane-wave basis projector augmented wave as implemented in the Vienna ab-initio Simulation Package (VASP)[47,48] was employed in the framework of DFT. The generalized gradient approximation (GGA) in the Perdew-Burke-Ernzerhof form[45,46] and hybrid Heyd-Scuseria-Ernzerhof functional (HSE06)[49] were used for the exchange-correlation potential. The kinetic energy cutoff of 600 eV, and a Γ-centered $16\times16\times1$ k-mesh were employed in our calculations by using Monkhorst-Pack[50]. The tolerance of the total energy was converged to less than 10^{-5} eV with forces less than 10^{-3} eV Å^{-1}. The primitive unit cells were used and the lattice constants and atomic positions were optimized without any constraint. A vacuum space $\sim$ 20 Å along the z-direction was used to avoid any fictitious interactions in MLs and HTS systems. Due to the interaction between the two layers, vdW interaction in the frame of Grimme (DFT-D2) method was utilized[51]. The Bader charge analysis[52] was utilized to extract the electronic charge transfers. The vibrational properties were computed by the finite-displacement method implemented in the PHONOPY code[53]. The optical spectra were performed in the random phase approximation[?] method constructed over HSE06 using a dense k-grid of $20\times20\times1$. The wave function in the interstitial region was expanded in terms of plane waves with a cut-off parameter of R_{MT} K_{max}= 8.5, where R_{MT} and K_{max} denote the smallest atomic sphere radius and the largest k vector, respectively.

3 Monolayers

The atomic structures, contour plot of the electron localization function (ELF) and electronic structure with the corresponding partial density of states (PDOS) of MoS_2 and $MoSi_2N_4$ monolayers are shown in Fig. 1. From the atomic structures of the MoS_2 and $MoSi_2N_4$, the atoms are packed in a honeycomb lattice, forming a 2D crystal with a space group of P_{6m1}. The hexagonal primitive unit cell indicated by red parallelogram. After structure optimization, the lattice constants are 3.21 Å and 2.91 Å for MoS_2 and $MoSi_2N_4$, respectively. The bond lengths of Mo-S is 2.58 Å and the S-Mo-S angle is 77.36°. For $MoSi_2N_4$ the bond lengths of Mo-Si, Mo-N and Si-N are 2.09 Å, 1.75 Å and 1.74 Å, respectively. The two angles of Si-N-Si are 112 ° and 106°, while the two angles of Si-Mo-Si are 87 ° and 73°. The thickness of the MoS_2, the vertical distance of S-S is 2.99 Å and for $MoSi_2N_4$ is 7.01 Å. The structural results are in good agreement with the previous reports[31,39,40,44].

The cohesive energy (E_{coh}) per atom is calculated by: $E_{coh} = \frac{E_{Mo}+2E_{Si}+4E_N-E_{tot}}{n_{tot}}$ where E_{Mo}, E_{Si} and E_N, E_{tot} represent the energies of isolated Mo, Si, N atoms and total energy of the MLs, n_{tot} is the total number of atoms in the unit cell, respectively. The cohesive energy are found to be -5.61 eV/atom for MoS_2 and -38.46 eV/atom for $MoSi_2N_4$. The negative energy indicates the stability of structures. The contour plot of the electron localization function (ELF) is shown in Figs. 1(b,e). For the $MoSi_2N_4$, the negatively charged N atoms are surrounded by positively charged Si and Mo atoms due to a charge transfer from Si and Mo atoms to N

Table 1 The structural and electronic parameters including lattice constant **a**; the bond lengths of Mo-S (d_1), Mo-Si (d_2), Si-N (d_3), and Mo-N (d_4) ; the bond angles of S-Mo-S (θ_1), N-Si-N (θ_2) and N-Mo-N (θ_3); the thickness layer (t); the cohesive energy per atom, (E_{coh}) for the monolayers and binding energy for the HTS (E_b); the work function (Φ); the band gap (E_g) of PBE (HSE06); VBM/CBM positions.

	a (Å)	d_1 (Å)	d_2 (Å)	d_3 (Å)	d_4 (Å)	t (Å)	θ_1 (°)	θ_2 (°)	θ_3 (°)	E_{coh} (eV/atom)	Φ (eV)	E_g (eV)	VBM/CBM
MoS_2	3.21	2.58	-	-	-	2.99	77.36	-	-	-5.61	5.66	1.65 (2.14)	Γ/K
$MoSi_2N_4$	2.91	-	2.09	1.75	1.74	7.01	-	112,106	73,87	-8.46	5.12	1.79 (2.35)	Γ/K
$MoS_2/MoSi_2N_4$	2.96	2.37	2.10	-	3.46	13.59	77.38	113.03	71.32	-9.87	5.04	1.26 (1.84)	Γ/K

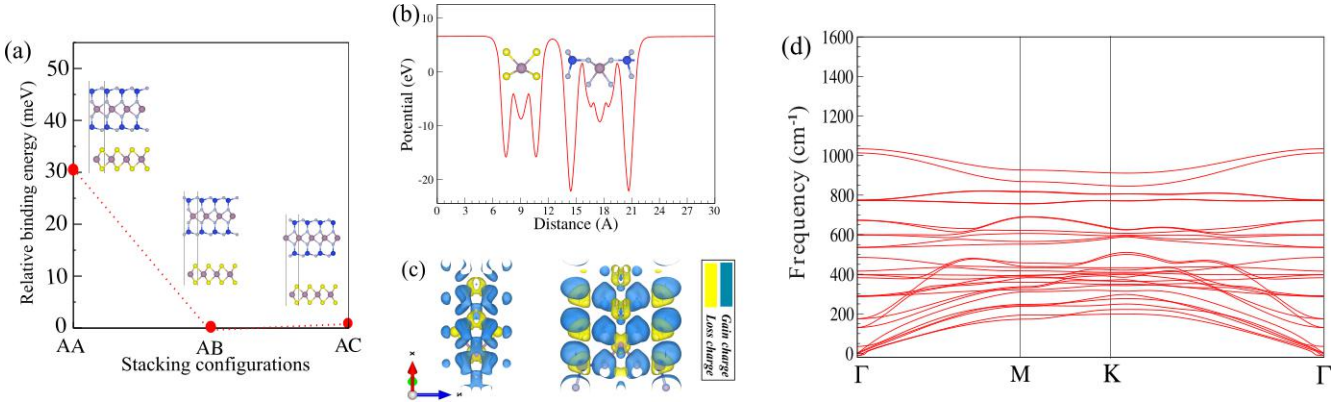

Fig. 2 (a) Relative binding energy for different stacking, (b) potential average per distance, (c) difference charge density per distance, (d) phonon band dispersion for $MoS_2/MoSi_2N_4$ heterostructure.

atom. While in the MoS_2, the negatively charged S atoms are surrounded by positively charged Mo atoms due to a charge transfer from Mo atoms to S atom The Bader charge analysis shows that in the $MoSi_2N_4$ each N atom gains 1.5e and 2.23e from the adjacent Mo and Si atoms, respectively. For MoS_2 each S atom gains 0.5e from the adjacent Mo atom. The work function (Φ) depends on the energy of the vacuum energy (E_{vacuum}) and the Fermi energy (E_F), $\Phi = E_{\text{vacuum}} - E_{\text{F}}$. We find Φ equals 5.66 eV for MoS_2 and 5.12 eV for $MoSi_2N_4$.

The electronic band structures with the corresponding density of states (DOS) and projected DOS (PDOS) of MoS_2 and $MoSi_2N_4$ are shown in Figs. 1(c) and (f), respectively. Our results show that the MoS_2 is an indirect semiconductor with a band gap of 1.65 eV (2.14 eV) , within PBE (HSE06) functional. The valence band maximum (VBM) and conduction band minimum (CBM) are located at the Γ and the K-point, respectively. The $MoSi_2N_4$ is a semiconductor with an indirect band gap of 1.79 eV (2.35 eV), within PBE (HSE06) functional and notice that the VBM and CBM are located at the Γ and the K-point, respectively. The charge density of the VBM and CBM orbitals is shown in the inset Fig. 1(f). The VBM is mainly originate by Mo-d_{z^2} and Mo-$d_{x^2-y^2}$ orbital states with a minor contribution of Si-p_z and N-p_z orbital states, representing σ(Mo-Mo) bonding hybridized with σ(N-Si) bonding. While the CBM is solely contributed by Mo-d_{z^2} orbital states representing a σ(Mo-Mo) bonding. Our results are in good agreement with previous calculations[31,39,40,44].

4 Heterostructure

4.1 Structure and Stability

The stacking of the $MoS_2/MoSi_2N_4$ heterostructure vertically using several stacking geometries, i.e. AA, AB and AC is shown in Fig. 2(a). The binding energy E_b is used to examine the energetic stablility of the MS/MSiN, $E_{\text{b}} = E_{\text{tot}} - E_{\text{MSiN}} - E_{\text{MS}}$, where E_{tot}, E_{MSiN}, and E_{MS} denotes the total energies of the MS/MSN, isolated $MoSi_2N_4$, and isolated MoS_2, respectively. Here after, the $MoS_2/MoSi_2N_4$ heterostructure is labeled as MS/MSiN. The calculated binding energy shows that the minimum energy configuration is the AB-stacking, where E_b=-9.87 eV. The heterostructure is exothermic and negative sign of binding energy refers to the thermodynamic stability. The relative binding energy of MS/MSiN for different stacking configuration is shown in Fig. 2(a). The structure parameters including lattice constant, bond length, bond angles of MS/MSN are given in table I. Notice that the interlayer distance is obtained as 3.21 Å, which is much larger than the sum of the covalent radii of N and S atoms, while the interface is dominated by vdW interactions.

The planar average electrostatic potential for the MS/MSiN is shown in Fig. 2(b). The electrostatic potential of studied monolayers are flat in the vacuum region. One can see that the symmetric potential behavior for individual layer due to the symmetric structure of monolayer. The electrostatic potential energy at S atomic layer is higher than that at Si atomic layer due to the higher electronegativity of S as compared to Si. The calculated work function for the HTS is 5.04 eV which is smaller than the corresponding value of $MoSi_2N_4$ and MoS_2 monolayers. This means the electrons in the MS/MSiN have the ability to escape from the

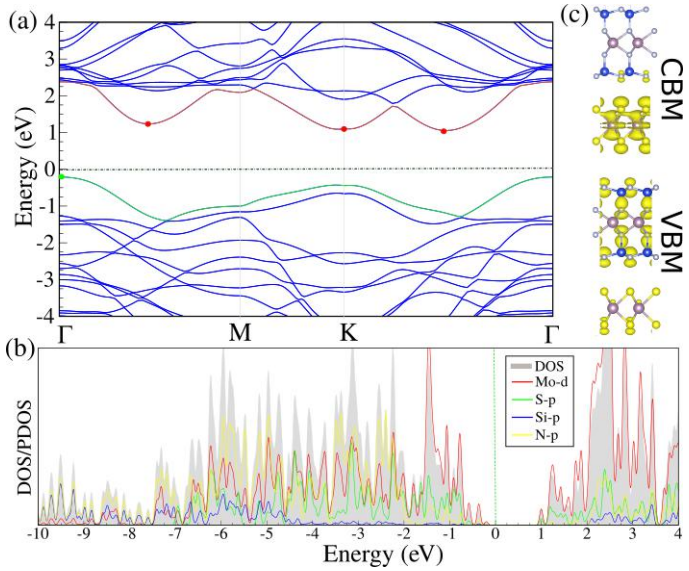

Fig. 3 (a) Electronic band structure and (b) DOS and PDOS and (c) charge densities of VBM and CBM orbitals of $MoS_2/MoSi_2N_4$ HTS. The zero of energy is set to Fermi-level.

surface more than its indvidual monolayer surfaces under applied field. The phonon dispersion is calculated to investigate the dynamical stability as is shown in Fig. 2(c). Apparently, phonon branches are free from any imaginary frequencies indicating the dynamical stability of the MS/MSiN.

4.2 Electronic properties

The electronic band structure with the corresponding DOS and PDOS of MS/MSiN is shown in Figs. 3(a,b). Our results show that, MS/MSiN is an indirect semiconductor with a band gap of 1.26 eV (PBE functional). Notice that the valance band minimum (VBM) is located at the Γ point, while the conduction band maximum (CBM) is located along the k-Γ points. Since these monolayers are semiconductor, the HSE06 functional was also used to study the electronic band structures. It is clear that the HSE06 results are consistent with PBE/GGA for the type of indirect semiconducting band gap in these systems. Based on the HSE06 method, the indirect band-gap of MS/MSiN is 1.84âĂŕeV. Due to the interaction between the two monolayers, the VBM of HTS is higher (lower) than the corresponding value of MS (MSiN) monolayer. On the other hand the CBM of HTS is lower than the corresponding value of MS and MSiN monolayers. Therefore the bandgap of HTS is smaller than the bandgap of its individual monolayers. In order to explain the origin of the electronic states, the DOS/PDOS of MS/MSiN is shown in Fig. 3(b). The Mo-d states are dominated from -2.2 eV to the higher energy. The N-p states are dominated in many ranges below -2.3 eV with good contributions from Mo-d and S-p states. The contribution of Si-p states is small as compared to the other states. The charge densities of the VBM and CBM orbitals are shown in Fig. 3(c). One can observe that the VBM of such heterostructure is distributed in the side of MSiN layer, whereas its CBM is localized in the side of MS layer.

4.3 Optical properties

To understand the optical properties of $MoS_2/MoSi_2N_4$ HTS, we calculated the dielectric constants of its individual monolayers (MLs) as shown in Figs. 4(a,b). The x and y components of the real part of dielectric constants are the same for monolayers and HTS. There are many peaks in the wavelength range 10-180 nm for x and y components. For z component there are only distinct peaks at 40 nm and 60 nm (Figs. 4(a)). The corresponding real dielectric constants as function in the incident energy is shown as the inset figure. The real dielectric constant of MS/MSiN is related to the dielectric constant of its MLs with a small shift of peak positions. The static dielectric constants of the HTS, the real dielectric constant at zero energy, are 8.5 for x and y components, and 4.2 for z component which are larger than the corresponding values for individual MLs (the inset of Figs. 4(a)). The imaginary part of the dielectric constant, Fig. 4(b), shows the x and y components are similar (as in the real component). There are many peaks for MLs and HTS in the wavelength range from 0 to 300 nm. The main peaks for MS and MSiN locate at 100 nm while the main peak for HTS locates at 80 nm. For z component, all peak positions locate at 50 nm. The imaginary dielectric constants as function in the energy are shown as the inset figure.

The absorption spectra of MoS_2, $MoSi_2N_4$ and HTS are shown in Fig. 4(c). The spectra are very related to the imaginary part of dielectric constants (Fig. 4(b)). The positions of the main peaks are very similar to the corresponding peak positions of the imaginary part of dielectric constants for all components. The absorption values of the HTS are higher than the corresponding values of MS and MSiN monolayer in the range of 0-300 nm for x and y components and in the whole range in the z component. Therefore the HTS can enhance the absorption of light not only in the ultraviolet region but also in the visible region. The absorption coefficient as a function in the energy is shown as the inset Fig. 4(c).

Fig. 4(d) shows the refractive index of the HTS as compared to the refractive indices of its monolayer components. The combination between the refractive indices of MS and MSiN monolayers gives the refractive index of the HTS in all directions. Therefore the refractive index of the HTS is larger than the refractive index of its MLs in the shown wavelength range. The static refractive index for HTS is 4.1 for x and y components and 3.2 for z component. The refractive index in the visible region 650 nm (2.2 eV) is 3.2 for x and y components and 2.1 for z component. The absorption spectra and refractive index of MoS_2 ML have a good agreement with the previous publications[54,55].

5 Conclusion

In conclusion, we investigated the electronic and optical properties of the $MoS_2/MoSi_2N_4$ heterostructure using first-principle calculations. The stability of the heterostructure is verified by calculating the phonon dispersion curves and thermodynamic binding energy calculations. Due to different monolayers, the electrostatic potential is asymmetric. The calculated work function of heterostructure is less than the corresponding values of its individual monolayers. The valance band maximum of heterostructure is very similar to the corresponding one of MoS_2 monolayer.

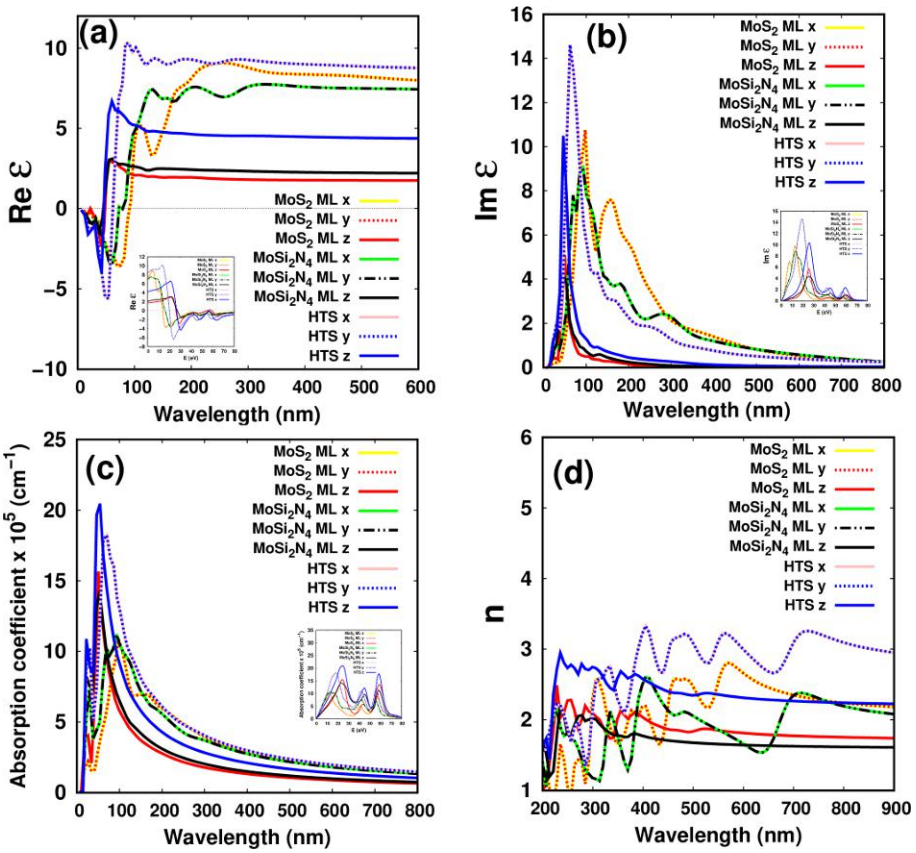

Fig. 4 (a) Real part of dielectric constant, (b) imaginary part of dielectric constant, (c) absorption and (d) refractive index of the MoS_2, $MoSi_2N_4$ and $MoS_2/MoSi_2N_4$ HTS at different applied electric field.

However the conduction band minimum is not similar to the corresponding one of MoS_2 and $MoSi_2N_4$ monolayers. The heterostructure and its monolayers have indirect gaps. The bandgap of $MoS_2/MoSi_2N_4$ is smaller than the bandgap of its monolayers using PBE and HSE06. The optical absorption values of the heterostructure are higher than its individual monolayers absorption. The refractive index of heterostructure can be understood in terms of a combination of the refractive indexes of its monolayers.

6 Conflicts of interest

The authors declare that there are no conflicts of interest regarding the publication of this paper.

7 ACKNOWLEDGMENTS

This work was supported by the National Research Foundation of Korea (NRF) grant funded by the Korea government (MSIT) (NRF-2015M2B2A4033123).

References

1 H. Li, J. Wu , Z. Yin H. Zhang, Acc. Chem. Res. 47 (4) (2014) 1067-1075.

2 W. Su , H. Dou , J. Li , D. Huo , N. Dai, L. Yang, RSC Adv. (2015) 82924-82929.

3 M. Buscema , G. A. Steele , H. S. J. van der Zant, A. Castellanos-Gomez, Nano Res. 7 (2014) 561-571.

4 W. Su , H. Dou , D. Huo , N. Dai, L. Yang, Chem. Phys. Lett. 635 (2015) 40-44.

5 S. Mouri , Y. Miyauchi K. Matsuda, Nano Lett. 13 (2013) 5944-5948.

6 X. Zhou , W. Feng , S. Guan , B. Fu , W. Su, Y. Yao, J. Mater. Res. 32 (2017) 2993-3001.

7 Y. Deng , Z. Luo , N. J. Conrad , H. Liu , Y. Gong , S. Najmaei , P. M. Ajayan , J. Lou , X. Xu, P. D. Ye, ACS Nano, 8 (2014) 8292-8299.

8 Y. Chen, T. Shi, P. Liu, X. Ma, L. Shui, C. Shang, Z. Chen, X. Wang, K. Kempa, G. Zhou, J. Mater. Chem. A 6 (2018) 19167-19175.

9 H. Shu, Y. Tong, J. Guo, Phys. Chem. Chem. Phys. 19 (2017) 10644-10650.

10 Z. Cui, K. Bai, Y. Ding, X. Wang, E. Li, J. Zheng, Physica E 123 (2020) 114207.

11 Z. Cui, K. Bai, Y. Ding, X. Wang, E. Li, J. Zheng, S. Wang, Superlattices Microstruct. 140 (2020) 106445.

12 Z. Guan, C.-S. Lian, S. Hu, S. Ni, J. Li, W. Duan, J. Phys. Chem. C 121 (2017) 3654-3660.

13 Z. Zhang, C. Shao, S. Wang, X. Luo, K. Zheng, H.M. Urbassek, Crystals 9 (2019) 584.

14 S. Wang, C. Ren, H. Tian, J. Yu, M. Sun, Phys. Chem. Chem. Phys. 20 (2018) 13394-13399.

15 M. M. Obeid, A. Bafekry, S. U. Rehman, C. Nguyen, Appl.

Surf. Sci. 534 (2020) 147607.
16 J. Yan, Y. Hao, Y. Cui, J. Zhang, Y. Zou, W. Zhang, G. Yu, J. Zheng, W. Xu, D. Zhu, J. Mater. Chem. C 2018, 6, 12976 -12980.
17 K. H. Chan , S. M. Ng , H. F. Wong , C. W. Leung, C. L. Mak, Phys. Status Solidi A 216 (2019) 1800829.
18 H. T. T. Nguyen ,M. M. Obeid , A. Bafekry, M. Idrees, T. V. Vu, H. V. Phuc ,N. N. Hieu, L. T. Hoa, B. Amin , C. V. Nguyen, Phys. Rev. B 102 (2020) 075414.
19 K. S. Novoselov, A. K. Geim, S. V. Morozov, D. Jiang, Y. Zhang, S. V. Dubonos, I. V. Grigorieva, A. A. Firsov, Sci. 306 (2004) 666-669.
20 G. Fiori, F. Bonaccorso, G. Iannaccone , T. Palacios , D. Neumaier, A. Seabaugh, S. K. Banerjee, L. Colombo, Nat. Nanotechnol. 9(10) (2014) 768-779.
21 Y.-Q. Bie, G. Grosso, M. Heuck, M. M. Furchi, Y. Cao, J. Zheng, D. Bunandar, E. Navarro-Moratalla, L. Zhou, D. K. Efetov, T. Taniguchi, K. Watanabe, J. Kong, D. Englund, P. Jarillo-Herrero Nat. Nanotechnol. 12 (2017) 1124-1129.
22 F. Xia, H. Wang, D. Xiao, M. Dubey, A. Ramasubramaniam, Nat. Photon. 8 (2014) 899-907.
23 Y. Ye, J. Xiao, H. Wang, Z. Ye, H. Zhu, M. Zhao, Y. Wang, J. Zhao, X. Yin, X. Zhang, Nat. Nanotechnol. 11(7) (2016) 598-602.
24 E. Pomerantseva, Y. Gogotsi, Nat. Energy 2 (2017) 17089.
25 A. Bafekry, C. Stampfl, M. Ghergherehchi, Nanotechnol. 31 (2020) 295202.
26 K. Huang, Z. Li, G. Han, P. Huang, Chem. Soc. Rev. 47 (2018) 5109-5124.
27 Y. Liu, D. Tian, A. N. Biswas, Z. Xie, S. Hwang, J. H. Lee, H. Meng, J. G. Chen, Angew. Chem. Int. Ed. 59(28) (2020) 11345-11348.
28 P. Eklund, S. Kerdsongpanya, B. Alling, J. Mater. Chem. C 2016, 4, 3905-3914
29 A. Salamat, A. L. Hector, P. Kroll, P. F. McMillan, Chem. Rev. 257 (2013) 2063-2072.
30 M. Sarwan, V. A. Shukoor, S. Singh, AIP Conf. Proc. 1953 (2018) 040018.
31 A. Bafekry, M. Yagmurcukardes, B. Akgenc, M. Ghergherehchi, C. Nguyen, J. Phys. D: Appl. Phys. 53 (2020) 355106.
32 A.O.M. Almayyali, B.B. Kadhim, H.R. Jappor, Phys. E: Low-dimen. Sys. Nanost. 118, (2020) 113866.
33 A.O.M. Almayyali, B.B. Kadhim, H.R. Jappor, Chem. Phys. 532, (2020) 110679.
34 M.M. Obeid, A. Bafekry, S.U. Rehman, C.V. Nguyen, Appl. Surf. Sci. 534, (2020) 147607.
35 A. Bafekry, M. M. Obeid, C. Nguyen, M.B. Tagani, M. Ghergherehchi, J. Mater. Chem. A 8, (2020) 13248-13260.
36 A. Bafekry, M. Yagmurcukardes, M. Shahrokhi, M. Ghergherehchi, Carbon 168, (2020) 220-229.
37 A. Bafekry, M. Neek-Amal, Phys. Rev. B 101 (2020), 085417.
38 A. Bafekry, B. Akgenc, S.F. Shayesteh, B. Mortazavi, Appl. Surf. Sci. 505, (2020) 144450.
39 Y.-L. Hong, Z. Liu, L. Wang, T. Zhou, W. Ma, C. Xu, S. Feng, L. Chen, M.-L, Chen, D.-M. Sun, X.-Q. Chen, H.-M. Cheng, W. Ren, Sci. 369 (2020) 670-674.
40 A. Bafekry, M. Faraji, D. M. Hoat, M. M. Fadlallah, M. Shahrokhi, F. Shojaei, D. Gogova, M. Ghergherehchi, J. Phys. D: Appl. Phys. 54 (2021), 155303
41 Y. S. Ang, H. Y. Yang, and L. K. Ang, Phys. Rev. Lett. 121 (2018) 056802.
42 D. S. Schulman, A. J. Arnold, S. Das, Chem. Soc. Rev. **47**, 3037 (2018).
43 S. Banerjee, L. Cao, Y. S. Ang, L. K. Ang, P. Zhang, Phys. Rev. Appl. **13**, 064021 (2020).
44 L. Cao, G. Zhou, L. K. Ang, Y. S. Ang, Appl. Phys. Lett. **118**, 013106 (2021).
45 J. P. Perdew, K. Burke, and M. Ernzerhof, Phys. Rev. Lett. **77**, 3865 (1996).
46 J. P. Perdew, K. Burke, and M. Ernzerhof, Phys. Rev. Lett. **78**, 1396 (1997).
47 G. Kresse and J. Hafner, Phys. Rev. B **47**, 558 (1993).
48 G. Kresse and J. Hafner, Phys. Rev. B **49**, 14251 (1994).
49 J. Heyd, G. E. Scuseria, and M. Ernzerhof, J. Chem. Phys. **118**, 8207 (2003).
50 H.J. Monkhorst and J.D. Pack, Phys. Rev. B **13**, 12, (1976).
51 S. J. Grimme, Comput. Chem. **27**, 1787 (2006).
52 G. Henkelman, A. Arnaldsson, and H. Jonsson, Comput. Mater. Sci. **36**, 354 (2006).
53 D. Alfe, Comput. Phys. Commun. **180**, 2622 (2009).
54 Qiu, Bin and Zhao, Xiuwen and Hu, Guichao and Yue, Weiwei and Ren, Junfeng and Yuan, Xiaobo, Nanomaterials **8**, 11 (2018).
55 Kravets, Vasyl G., Wu, Fan, Auton, Gregory H., Yu, Tongcheng, Imaizumi, Shinji, Grigorenko, Alexander N., NPJ 2D Materials and Applications **3**, 36 (2019).